Science Bulletin 64 (2019) 705–714

Contents lists available at ScienceDirect

Science Bulletin

journal homepage: www.elsevier.com/locate/scib

Science Bulletin
www.scibull.com

Article

Environmentally responsive dual-targeting nanotheranostics for overcoming cancer multidrug resistance

Caixia Yang [a,1], Xin Pang [a,1], Weihai Chen [b], Xiaoyong Wang [a], Gan Lin [a], Chengchao Chu [a], Xianzheng Zhang [b], Xianming Deng [c], Xiaoyuan Chen [d], Gang Liu [a,c,*]

[a] State Key Laboratory of Molecular Vaccinology and Molecular Diagnostics and Center for Molecular Imaging and Translational Medicine, School of Public Health, Xiamen University, Xiamen 361102, China
[b] Key Laboratory of Biomedical Polymers of Ministry of Education & Department of Chemistry, Wuhan University, Wuhan 430072, China
[c] State Key Laboratory of Cellular Stress Biology, Innovation Center for Cell Signaling Network, School of Life Sciences, Xiamen University, Xiamen 361102, China
[d] Laboratory of Molecular Imaging and Nanomedicine, National Institute of Biomedical Imaging and Bioengineering (NIBIB), National Institutes of Health (NIH), Bethesda, MD 20892, USA

ARTICLE INFO

Article history:
Received 19 January 2019
Received in revised form 10 March 2019
Accepted 4 April 2019
Available online 12 April 2019

Keywords:
Cancer chemosensitization
Multidrug resistance
P-glycoprotein
pH-responsive
Magnetic resonance imaging

ABSTRACT

The development of multiple drug resistance (MDR) to chemotherapy and subsequent treatment failures are major obstacles in cancer therapy. An attractive option for combating MDR is inhibiting the expression of P-glycoprotein (P-gp) in tumor cells. Here, we report a novel chemosensitizing agent, XMD8-92, which can down-regulate P-gp. To enhance the specificity of MDR chemotherapy, a promising nanotheranostic micelle system based on poly(ethylene glycol)-blocked-poly(*L*-leucine) (PEG-*b*-Leu) was developed to simultaneously carry the anticancer drug doxorubicin, chemosensitizing agent XMD8-92, and superparamagnetic iron oxide nanoparticles (SPIOs). Featured with MDR environmentally responsive dual-targeting capability, controllable drug delivery, and efficient magnetic resonance (MR) imaging characteristics, the prepared nanotheranostics (DXS@NPs) showed outstanding in vitro cytotoxicity on MDR cells (SCG 7901/VCR) with only 53% of cells surviving compared to 90% of DOX-treated cells. Furthermore, efficient tumor inhibition and highly reduced systemic toxicity were exhibited by MDR tumor-bearing mice treated with DXS@NPs. Overall, the environmentally responsive dual-targeting nanotheranostics represent a promising approach for overcoming cancer MDR.

1. Introduction

Chemotherapy is commonly used to treat cancer, either alone or in combination with radiotherapy or surgery. However, the development of cancers with multiple drug resistance (MDR) to chemotherapeutic agents and the subsequent treatment failures are seriously impeding the effectiveness of cancer chemotherapy in clinic [1,2]. Various biological events are attributed to the establishment of a MDR phenotype, but for most of the MDR cancer cells, the over-expression of P-glycoprotein (P-gp) is the chief culprit [3]. As a member of the ATP-binding cassette (ABC) superfamily, P-gp can efficiently expel a wide spectrum of chemotherapeutic agents out of cells, thereby decreasing their intracellular accumulation and therapeutic potency [4–6]. Hence, pharmacological inhibition of specific ABC transporters, especially P-gp, has been identified as a promising way to combat MDR. Recently, several inhibitors and modulators of ABC transporters have been developed, but high toxicity and unfavorable pharmacokinetic interactions have prohibited their use [7]. The search for novel inhibitors and modulators to combat MDR is still ongoing. Interestingly, we have recently found that XMD8-92, in addition to serving as a big mitogen-activated protein kinase 1 (BMK1) inhibitor to target p53 up-regulation, can efficiently down-regulate P-gp expression [8–12]. This rather unexpected finding implies that the combination of XMD8-92 with traditional chemotherapeutic agents may represent a promising new approach toward enhancing the susceptibility of MDR cancer cells to chemotherapy.

However, the P-gp transporters are also a crucial defense line to protect the cells and organisms via efflux of xenobiotics. Therefore, inhibition of P-gp expression may enhance the delivery of harmful xenobiotics to the unaffected organs, which may lead to increased intracellular accumulation of toxins. How to specifically deliver anticancer therapeutics and their sensitizers to tumor sites and effectively reduce the exposure of healthy tissues is a major

* Corresponding author.
E-mail address: gangliu.cmitm@xmu.edu.cn (G. Liu).
[1] These authors contributed equally to this work.

https://doi.org/10.1016/j.scib.2019.04.019
2095-9273/

challenge facing MDR cancer treatment. Toward this end, nanotechnology brings a new era in cancer research since it revolutionizes both the diagnosis and treatment by refining tumor-specific targeting [13–15]. Recent studies have suggested that nanomedicine offers great promise for eradicating MDR by increasing and tailoring the intracellular delivery of therapeutic agents [6,16–22]. Compared to the traditional chemotherapy, nano-based delivery systems make it accessible to co-load chemotherapeutic compounds and chemosensitizing agents, including transporter protein inhibitors or gene-silencing agents, into one nanocarrier [23–30]. With continued elaborate engineering, through chemical modification or physical coating, such nano delivery systems can be tailored to serve a wealth of functions, such as active tumor targeting, environmentally-responsive drug release, and image-guided cancer theranostics [31–33]. Consequently, it is available to realize enhanced specificity to tumor sites, improved therapeutic index of MDR cancer, as well as decreased toxicity.

In this context, a multifunctional drug delivery system (DDS) based on poly(ethylene glycol)-blocked-poly(*L*-leucine) (PEG-*b*-Leu) micelles was developed for cancer imaging and chemotherapy (Scheme 1). The hydrophobic *L*-leucine core provides ample space for drug loading and the hydrophilic PEG shell improves the stability of PEG-*b*-Leu micelles and prolongs their blood circulation time [34–36]. As a commonly used cancer-targeting moiety, biotin was incorporated into the PEG-*b*-Leu backbone for effective tumor localization and cellular uptake [37–39]. The chemotherapeutic drug doxorubicin (DOX), chemosensitizing agent XMD8-92, and magnetic resonance imaging (MRI) agent superparamagnetic iron oxide nanoparticles (SPIOs) were simultaneously loaded into the Biotin-PEG-*b*-Leu nanoparticles (DXS@NPs) through a simple one-step method and then were evaluated on MDR cancer cells (SCG 7901/VCR). Due to the pH-sensitivity of poly(*L*-leucine) which can be protonated in acidic conditions and then converted from hydrophobicity into hydrophilicity, the DXS@NPs rapidly dissociated to release encapsulated agents under the acidic tumor microenvironment. Further taking advantage of the passive enhanced permeability and retention (EPR) effect and active biotin-targeting in tumor tissue, a highly increased tumor accumulation was observed through MRI imaging. Compared to the cytotoxicity of free DOX, the DXS@NPs efficiently combatted drug resistance, providing more excellent in vitro inhibition on MDR SCG 7901/VCR cells. In vivo studies on MDR tumor-bearing mice further confirmed such potent MDR reversion and anticancer effects. Moreover, in addition to the widely reported function of p53 up-regulation, this study established XMD8-92 as a viable approach toward down-regulating P-gp expression.

2. Materials and methods

2.1. Materials

Doxorubicin hydrochloride (DOX·HCl) was purchased from Zhejiang Hisun Pharmaceutical Co., China. Biotin-poly(ethylene glycol)-NH_2-3400 (Biotin-PEG-NH_2) was brought from Laysan Bio Inc. Iron (III) acetylacetonate and XMD8-92 were obtained from Sigma-Aldrich (USA). Dulbecco's Modified Eagle's Medium (DMEM), Roswell Park Memorial Institute-1640 (RPMI-1640) medium, fetal bovine serum (FBS), trypsin, penicillin, streptomycin, 3-[4,5-dimethylthiazol-2-yl]-2,5-diphenyltetra-zoliumbromide (MTT), 4′,6-diamidino-2-phenylindole (DAPI) were purchased from Invitrogen. Rabbit anti-mouse P-gp antibody was obtained from Santa Cruz Biotechnology. All other reagents and solvents were of analytical grade and used directly.

2.2. Synthesis and characterization

Biotin-PEG-*b*-Leu was synthesized according to our previous report [40]. ^{1}H nuclear magnetic resonance (^{1}H NMR) spectra of Leu-NAC and Biotin-PEG-*b*-Leu were recorded on a Varian Unity 300 MHz spectrometer. The molecular weight of Biotin-PEG-*b*-Leu was confirmed to be about 5,000 g/mol by gel-permeation chromatography (GPC) system consisting of Waters 2690D separations module and Waters 2410 refractive index detector (PDI = 1.20). Superparamagnetic iron oxide nanoparticles (SPIOs) nanocrystals were synthesized by thermal decomposition of iron (III) acetylacetonate. The DXS@NPs were prepared by mixing DOX, XMD8-92, SPIOs and Biotin-PEG-*b*-Leu in chloroform (5 mg DOX, 1 mg XMD8-92, 5 mg SPIOs, 5 mg Biotin-PEG-*b*-Leu in 500 μL chloroform) and then adding the mixed solutions into distilled water (5 mL) by droplets under sonication. Afterwards, the resulting solution was shook overnight to evaporate the chloroform and centrifuge at 12,000 r/min for 10 min to acquire the nanoparticles.

The particle size was measured using dynamic light scattering (DLS) (NanoZS 90, Malvern, USA) and transmission electron microscopy (TEM) (Tecnai G2 Spirit BioTwin, FEI, USA). The encapsulation efficiencies of DOX, XMD8-92, and SPIOs were determined using fluorescence microplate reader, high performance liquid chromatography (HPLC) (Ulti-Mate 3000, Dionex, USA) and inductively couple plasma mass spectrometry (ICP-MS) by measuring the unloaded drugs in the supernatant, respectively.

The MRI capacity of the DXS@NPs was verified at a 9.4 T MR scanner (Bruker 94/20 USR, Germany) at room temperature. DXS@NPs of different iron concentration ranging from 0.03 to 0.5 mmol/L were dispersed in 1% agarose gel, and T_2-weighted MR images were acquired using a fast spin-echo (FSE) sequence with the following parameters: repetition time/echo time (TR/TE) = 2,500/33 ms (T_2), 256 × 256 matrices.

2.3. In vitro drug release study

To measure in vitro drug release, DXS@NPs solutions were incubated in PBS (pH 5.5 and 7.4) at 37 °C in dialysis bags. The bags were immersed into 20 mL of PBS (pH 5.5 and 7.4) in a 50 mL centrifuge tube and kept shaking at 37 °C. Then the PBS was replaced with new one at selected time point. The DOX and XMD8-92 content was quantified with a fluorescence microplate reader and HPLC by comparing with a standard curve.

2.4. Cell culture

Drug-sensitive SCG 7901 cells were incubated in DMEM medium and multidrug-resistant counterpart SCG 7901/VCR cells were incubated in RPMI-1640 medium supplemented with 10% FBS and 1% antibiotics at 37 °C in a humidified atmosphere containing 5% CO_2. To maintain the resistant phenotype, SCG 7901/VCR cells were maintained in the medium containing 1 μg/mL vincristine and were cultured in drug-free medium for 48 h before the experiments.

2.5. In vitro cytotoxicity assay

MTT experiments were performed to confirm the sensitivities of the drug-sensitive SCG 7901 cells and drug-resistant SCG 7901/VCR cells, as well as the cytotoxicity of XMD8-92, DS@NPs (DOX and SPIO were co-encapsulated into Biotin-PEG-*b*-Leu), XS@NPs (XMD8-92 and SPIO were co-encapsulated into Biotin-PEG-*b*-Leu), DXS@NPs (DOX, XMD8-92 and SPIO were co-encapsulated into Biotin-PEG-*b*-Leu) on SCG 7901/VCR cells. SCG 7901 cells and SCG 7901/VCR cells were seed in 96-well plates at a density

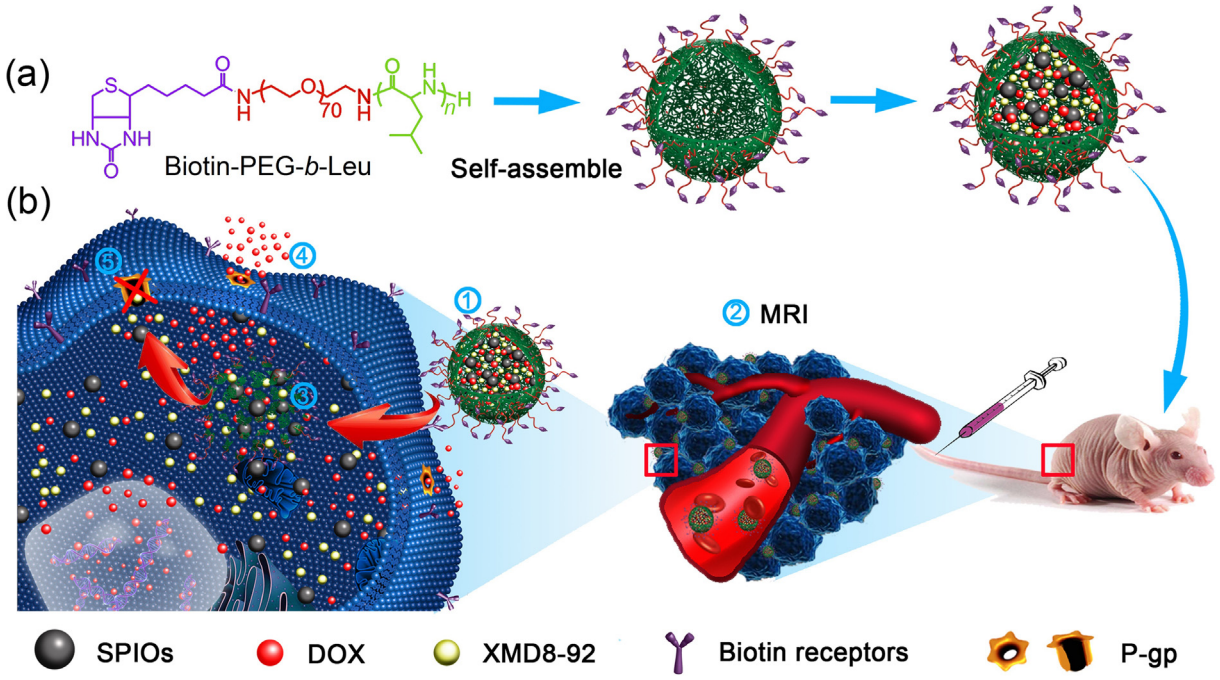

Scheme 1. (Color online) Schematic representation for DXS@NPs theranostic platform. (a) The preparation of DXS@NPs. (b) The use of DXS@NPs to image and treat MDR tumors. Long circulating DXS@NPs are passively localized in the tumor tissue via the EPR effect and active targeting ①, which could be used for further MRI ②. The release of DOX, XMD8-92 and SPIOs could be triggered by dissociation of DXS@NPs as a decrease of pH in the endosomes ③. DOX in the cytoplasm is expelled through P-gp in the cell membrane ④, while XMD8-92 could destroy P-gp and keep DOX inside tumor cells ⑤.

of 5,000 cells/well for 12 h incubation and then treated with different drugs for 72 h. After mixing with MTT solution (0.5 mg/mL) for 4 h, DMSO was added to dissolve the formazan crystals. The absorbance of the resulting solution was measured at a wavelength of 570 nm using a microplate reader (Thermo Multiskan Go, USA).

2.6. Cellular uptake and intracellular accumulation and retention of DOX

The cellular uptake of free DOX, DS@NPs, DXS@NPs and intracellular DOX accumulation and retention were investigated by laser scanning confocal microscope (CLSM) (FV1200, Olympus, Japan). Slides with SCG 7901/VCR cells were washed three times with PBS and immobilized with 4% polyformaldehyde after treatment with above solutions at 37 °C for 0, 4, 6, 24 h (DOX concentration: 2.3 μmol/L). The slides were further stained with DAPI and imaged under the CLSM.

2.7. Cancer cell targeted uptake

A competition assay was performed to confirm the cellular targeted efficiency of DXS@NPs. As experiment group, SCG 7901 cancer cells and GES normal cells were seeded on the slides and incubated with DXS@NPs (containing 2.3 μmol/L DOX) for 3 h. By contrast, cells in biotin block group were pre-treated with excess biotin (1 mmol/L) for 4 h in advance. Then the culture medium was replaced with new one and incubated with DXS@NPs (containing 2.3 μmol/L DOX). After 3 h, the cells were washed three times with PBS and stained nuclei with DAPI. All slides were observed under the CLSM (FV1200, Olympus).

2.8. In vitro P-gp expression

The P-gp protein expression was analyzed by immunofluorescence, flow cytometry (FCM) and western blot experiments. To perform immunofluorescence staining, cells were seeded on slides, treated with different methods, and washed three times with PBS. After immobilization with 4% polyformaldehyde, thorough wash using PBS and block by 5% BSA, the slides were treated with rabbit anti-mouse P-gp antibody (1:200, Santa Cruz Biotechnology) overnight at 4 °C, followed by incubation with FITC goat anti-rabbit IgG (1:200; Santa Cruz Biotechnology) secondary antibodies for 1 h at 37 °C. After that, the slides were washed with PBS for three times, stained with DAPI and visualized under the CLSM (FV1200, Olympus).

The P-gp levels on the surface of cells were also measured by FCM (Cyan ADP, Beckman, USA). Cells with different therapies were collected, washed three times with PBS, and incubated with P-gp antibody (1:200, Santa Cruz Biotechnology, overnight at 4 °C) and appropriate FITC goat anti-rabbit IgG (1:1,000), Santa Cruz Biotechnology, 1 h at room temperature). After washing with cold PBS and filtering through 35 μm nylon mesh, the fluorescent intensity was examined on FCM and analyzed with FlowJo software.

Western blot experiment was performed as following procedures: cells samples were harvested after therapy and the proteins were subjected to 10% SDS-PAGE and transferred to polyvinylidene fluoride (PVDF) membranes (Millipore, Immobilon-P). After being blocked with 5% BSA, the membranes were incubated with diluted rabbit anti-mouse P-gp (1:1,000, Santa Cruz Biotechnology) and a monoclonal anti-β-actin antibody (1:1,000, Santa Cruz Biotechnology) at 4 °C overnight. After being washed with TBST for 3 times and further incubation with secondary antibodies, the membrane was visualized using Bio-Rad Chemi Doc XR + system.

2.9. In vitro magnetic resonance imaging

SCG 7901/VCR cells were seeded on 6-well plates (5×10^5 cells/well) and incubated with DXS@NPs of different SPIOs concentration (0, 1, 5, 10 μg/mL) for 24 h. Then the cells were trypsinized,

collected, and resuspended in 1% agarose gel for MRI analysis. The MRI analysis was carried out at a 9.4 T MR scanner (Bruker 94/20 USR, Bruker, Germany) at room temperature, and T_2-weighted MR images were acquired using a fast spin-echo (FSE) sequence with the following parameters: TR/TE = 2500/33 ms (T_2), 256 × 256 matrices, slice thickness = 1 mm.

2.10. Animal studies and tumor inoculation

Male Balb/c nude mice (6–8 weeks old) were cared in accordance with the Guidance Suggestions for the Care and Use of Laboratory Animals. To establish tumor model, about 10^7 SCG 7901/VCR cells were subcutaneously injected into the right forelegs. Around 10 d post-inoculation, the multidrug resistant tumor model was established. All animal experiments were approved by the Animal Management and Ethics Committee of Xiamen University.

2.11. In vivo MR imaging with DXS@NPs

In vivo MRI studies were performed with a 9.4 T imaging system (Bruker 94/20 USR, Bruker) using a mouse coil (Bruker) for transmission and reception of the signal. Multisection T_2-weighted FSE sequence (TR = 2,500 ms, TE = 33 ms; FOV = 40 mm × 40 mm; slice thickness 1 mm; flip angle 180) was used for all our studies. MRI scan was performed before and after DXS@NPs injection at a dose of 10 mg SPIOs/kg body weight.

2.12. In vivo tumor growth inhibition

When the tumors reached around 100 mm^3, the mice were randomly divided into four groups (five mice in each group) and intravenously injected with 100 μL of PBS, XS@NPs, free DOX and DXS@NPs at a DOX dosage of 5 mg/kg on day 1, 4, 7. The dosages of DOX in free DOX and XS@NPs groups were consistent with DXS@NPs group. The tumor volumes and body weights of various groups were measured every two days. The tumor volumes were calculated as follows: $V = L \times W^2/2$, where V is tumor volume, L is the tumor dimension at the longest point, and W is the tumor dimension at the widest point.

2.13. Immunohistochemistry analysis

Tumor sections obtained from SCG 7901/VCR tumor bearing mice with different therapies (PBS, free DOX, DS@NPs, DXS@NPs) were fixed in 4% polyformaldehyde and embedded in paraffin. Paraffin embedded tissue blocks were cut to 4 μm sections and dehydrated in xylene and graded alcohol. After antigen retrieval, 3% hydrogen peroxide was incubated with the slides for 30 min to inactivate endogenous peroxidase. Then the slides were blocked with goat serum to reduce nonspecific binding and then incubated with diluted P-gp antibody (1:200, Santa Cruz Biotechnology) at 4 °C overnight, followed by incubation with peroxidase-conjugated secondary antibody for 1 h. Diaminobenzidine (DAB) substrate and hematoxylin were used for detection and counterstaining respectively. All slides were reviewed under a microscope (Nikon, Ti-U).

2.14. Hematoxylin and eosin (H&E) stain of tissue sections

Major organs (heart, liver, spleen, lung, kidney) and tumors from the treatment groups and control group were collected and immediately fixed in 4% polyformaldehyde. The tissue sections were stained with hematoxylin and eosin stains according to standard histological protocols. All sections were examined under a Nikon microscope.

2.15. Statistical analysis

Data were reported as mean ± standard deviations. The differences among groups were determined using one-way ANOVA analysis. The differences were considered statistically significant when P values were 0.01 or less.

3. Results and discussion

3.1. Synthesis and characterization of DXS@NPs

As shown in Fig. S1 (online), the Biotin-PEG-*b*-Leu nanocarrier was synthesized through a multistep process and characterized by ^{1}H NMR (Fig. S2 online). The hydrodynamic size, determined by DLS, was around 105 nm in an aqueous solution (pH 7.4) (Fig. S3 online) and TEM image confirmed its spherical morphology (Fig. S4 online). Using self-assembling technology, the DXS@NPs were constructed by co-encapsulating DOX, XMD8-92, and SPIOs into the Biotin-PEG-*b*-Leu carrier. The TEM image in Fig. 1a showed that the SPIO clusters were successfully loaded into DXS@NPs, resulting in a significantly high r_2 value (322.8 Fe (mmol/L)$^{-1}$ s^{-1}) and low MRI signal intensity (Fig. 1b). The hydrodynamic size of the DXS@NPs indicated by DLS was around 91 nm (Fig. 1c), which was optimal for increased accumulation of DXS@NPs in tumor sites through the EPR effect. DS@NPs and XS@NPs were also prepared by encapsulating DOX and SPIOs or XMD8-92 and SPIOs into the Biotin-PEG-*b*-Leu carrier using the same method.

The encapsulation efficiencies of DOX, XMD8-92, and SPIOs were quantified with fluorescence microplate reader, high performance liquid chromatography (HPLC), and inductively coupled plasma mass spectrometry (ICP-MS) with 97%, 85%, and 62%, respectively. The drug release capacity of the DXS@NPs was determined in vitro at 37 °C in PBS buffer at two different pH values (pH 5.5 and 7.4) (Fig. 1d). Both DOX and XMD8-92 showed a pH-dependent release, which may be attributed to the increased protonation of the amino groups in Biotin-PEG-*b*-Leu under acidic conditions [41,42]. The release rates at pH 5.5 were much faster than at pH 7.4 with 56% and 28% of DOX and 53% and 23% of XMD8-92 released respectively after 24 h of incubation. Nanoparticles are generally internalized into the cells by endocytosis and end up in the slightly acidic environments of the endosomal and lysosomal vesicles (pH 4.5–6.0) of the tumor cells. This pH-dependent release behavior is expected to endow DXS@NPs with sufficient stability during transportation in the blood (pH 7.4) and efficient release in the tumor cells, both of which are necessary to improve chemotherapy efficacy and reduce off-target toxicity.

3.2. In vitro cytotoxicity, cancer-targeted cellular uptake and internalization of the DXS@NPs

To examine the cytotoxicity of DXS@NPs on the MDR cells, MTT assays were performed. Free DOX was incubated with drug-sensitive SCG 7901 cells and drug-resistant SCG 7901/VCR cells for 72 h to establish the sensitivity of the two cell lines (Fig. S5 online). Results showed that the SCG 7901 cells are much more sensitive to free DOX (IC_{50} = 0.08 μmol/L) than the SCG 7901/VCR cells (IC_{50} > 4.6 μmol/L). No cytotoxicity was observed for XMD8-92 or XS@NPs alone up to the concentration of 10 μmol/L on SCG 7901/VCR cells (Fig. S6 online).

The optimal proportion of free DOX and XMD8-92 in the particles was chosen based on cytotoxicity experiments (Fig. 2a). The free DOX concentration was fixed at 2.3 μmol/L according to previous results (Fig. S5 online), while the XMD8-92 concentration ranged from 0 to 5.0 μmol/L. The combined cytotoxicity was relatively high at 0.5 μmol/L of XMD8-92 (DOX 2.3 μmol/L). To confirm the

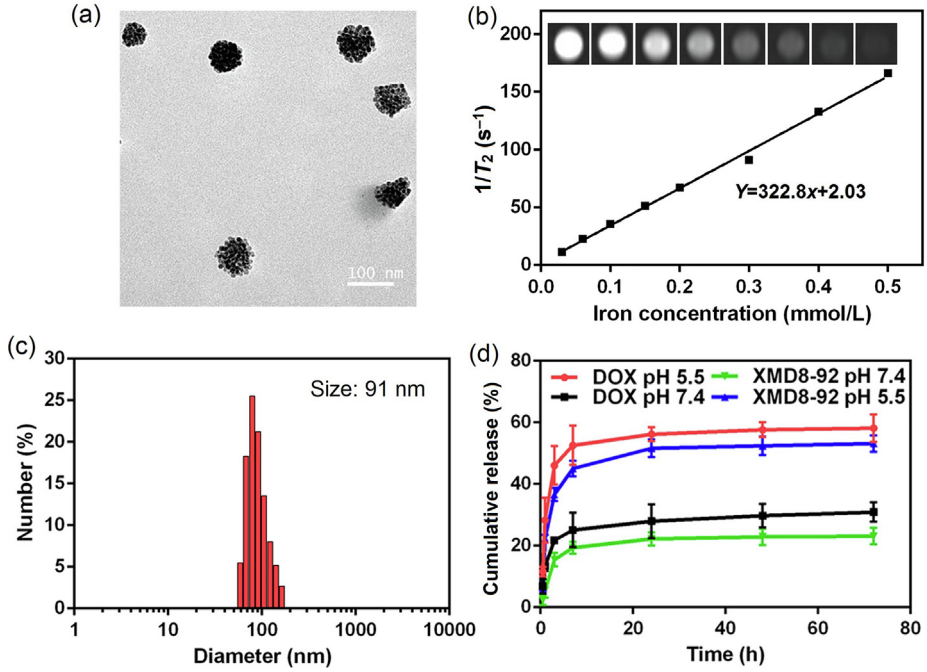

Fig. 1. (Color online) Characterization of DXS@NPs. (a) TEM image; (b) T_2 relaxation rate; (c) size distribution; and (d) drug release profiles of DXS@NPs. Scale bar: 100 nm.

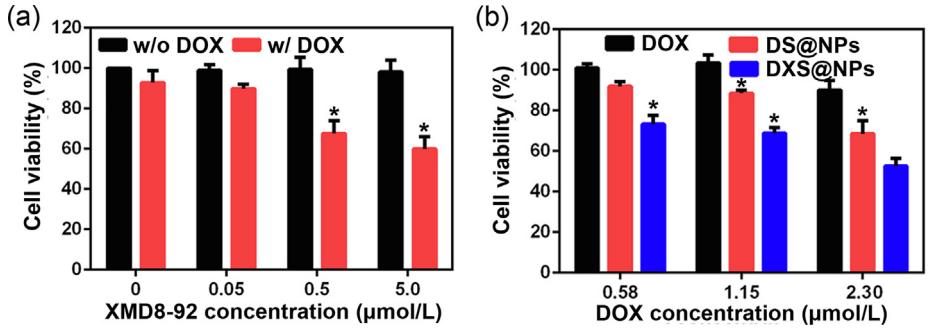

Fig. 2. (Color online) The cytotoxic experiments on SCG 7901/VCR cells. (a) The cytotoxicity of free DOX (2.3 μmol/L) and XMD8-92 (range from 0 to 5.0 μmol/L). (b) The cytotoxicity of free DOX (control group), DS@NPs, DXS@NPs solutions with equal DOX content. * means $P < 0.01$ compared to control group, one-way ANOVA.

inhibitory effect of the nanoparticles on the SCG 7901/VCR cells, free DOX, DS@NPs (containing DOX and SPIOs), and DXS@NPs (containing DOX, XMD8-92, and SPIOs) solutions were added to the MDR cells respectively at different DOX equivalent doses (0.58, 1.15, and 2.3 μmol/L) for 72 h (Fig. 2b). The cell viability decreased in a concentration-dependent manner. For example, about 90% of the SCG 7901/VCR cells were alive after incubation with free DOX at the concentration of 2.3 μmol/L, while only 69% and 53% cells survived when treated with DS@NPs and DXS@NPs respectively. The sensitivity of SCG 7901/VCR cells to DOX increased after DS@NPs treatment, likely due to the increased intracellular DOX concentration achieved by active targeting and the reduced drug efflux characteristic of nano-encapsulation. In contrast, the MDR cells exposed to DXS@NPs had the lowest resistance to DOX, which was attributed to the presence of XMD8-92 and the nanocarrier. These results suggest that DOX barely damages the MDR cells, while XMD8-92 greatly increased the cell susceptibility to DOX.

The cellular uptake and internalization of free DOX, DS@NPs, and DXS@NPs were investigated on SCG 7901/VCR cells at different time intervals (baseline, 1, 3, 6, and 12 h). The cells were fixed on slides, stained with DAPI, and then immediately imaged using CLSM (Fig. S7 online). The free DOX group showed faster fluorescence signal accumulation compared to the DXS@NPs group, peaking at 3 h, and then exported out of cells shortly, according to the quantitative analysis of intracellular DOX (Fig. S8 online). At 12 h, the intracellular DOX was greatly reduced in the free DOX and DS@NPs groups. However, the DXS@NPs group still exhibited relatively high DOX levels at 12 h, with a maximum accumulation at 6 h. This is most likely due to the faster diffusion of free DOX than the endocytosis-mediated processing of the DXS@NPs. Meanwhile, free DOX was efficiently exported by overexpressing P-gp, resulting in rapid intracellular DOX elimination. In the DXS@NPs group, the nanocarrier reduced this efflux and XMD8-92 decreased P-gp expression, jointly resulting in a higher intracellular concentration of DOX.

CLSM was used to establish the cancer-targeting ability of nanotheranostics. DXS@NPs was incubated with non-cancerous human gastric epithelial GES-1 cells (biotin receptor-negative) and cancerous SCG 7901 cells (biotin receptor-positive), which were pre-treated with or without free biotin for 6 h. Compared to the slight red fluorescent signal in the GES cells, the SCG 7901 cells showed considerable fluorescence from DOX (Fig. 3a), indicating that the nanoparticles were taken up more effectively by the

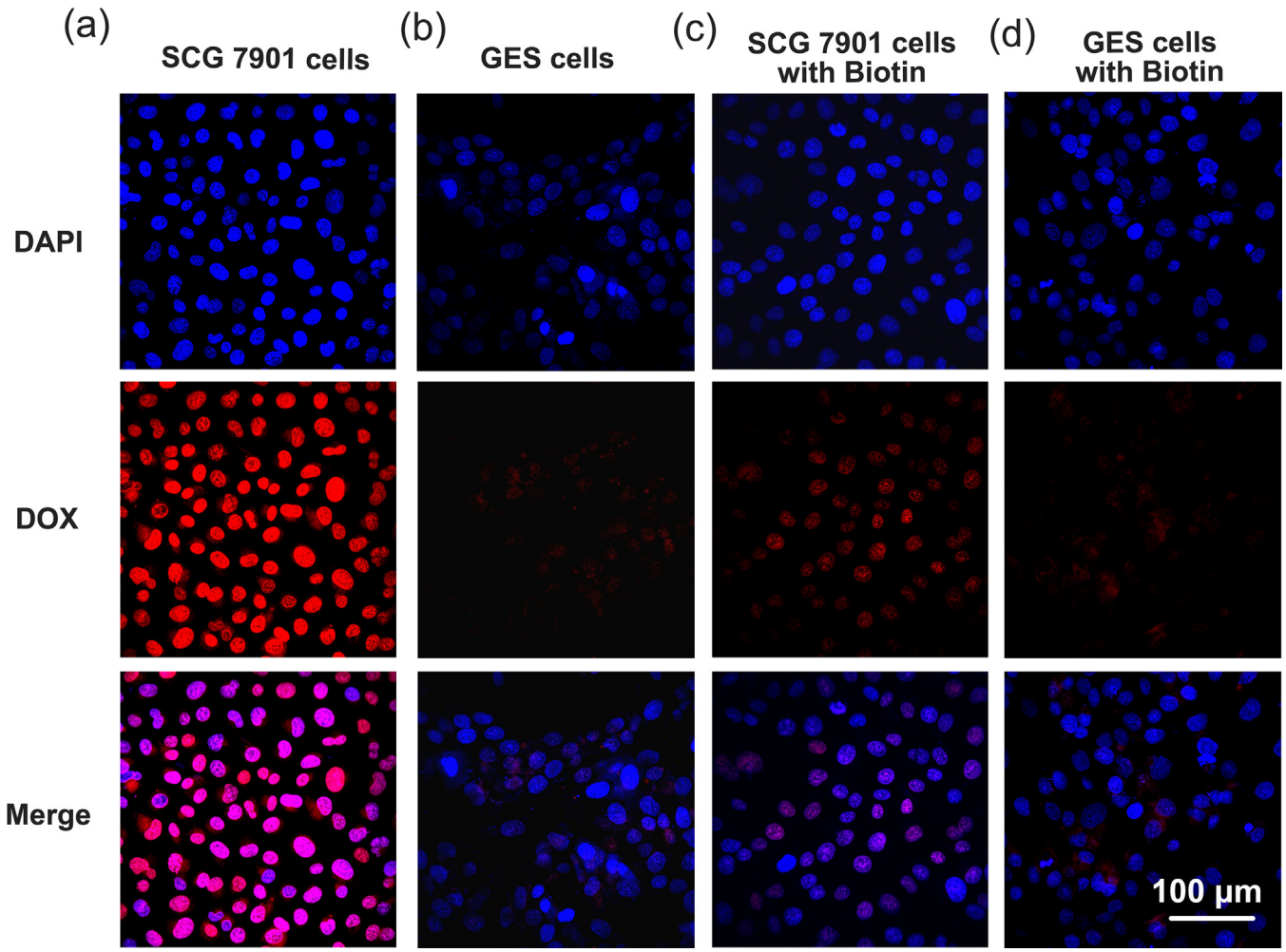

Fig. 3. (Color online) CLSM images of DXS@NPs incubated SCG 7901 and GES cells initially blocked with or without biotin (a–d). Scale bar: 100 μm.

cancerous cells (Fig. 3b). This increased intracellular uptake of nanoparticles was due to the active targeting ability of biotin on the surface of DXS@NPs [40]. To further confirm that the active targeting was mediated by the biotin receptor, cells were pre-treated with excessive free biotin to block its receptor. For the SCG 7901 cancer cells, the fluorescence intensity dropped dramatically relative to cells without biotin blocking treatment (Fig. 3c), while there was no obvious difference between the two conditions in the GES cell line, both of which had low fluorescence compared to the SCG 7901 cancer cells (Fig. 3d). The relative quantitative analysis of intracellular DOX also confirmed this result (Fig. S9 online).

3.3. In vitro P-gp detection

In order to confirm the elevated cytotoxicity of DXS@NPs caused by decreased expression of P-gp, three in vitro experiments were carried out including immunofluorescence, flow cytometry, and western blot analysis. Initially, SCG 7901/VCR cells, SCG 7901 cells, and DXS@NPs-treated SCG 7901/VCR cells were used for immunofluorescence analysis of P-gp after paraformaldehyde fixation (Fig. 4a–c). P-gp was overexpressed in SCG 7901/VCR cells compared to SCG 7901 cells, and the expression of P-gp was significantly reduced on the MDR cells after DXS@NPs treatment. Additionally, these cells were harvested and their P-gp contents were assessed using FCM (Fig. 4d–f). More P-gp expression was observed in the MDR cells than in the drug-sensitive SCG 7901 cells. For SCG 7901/VCR cells, treatment with DXS@NPs greatly reduced the number of P-gp positive cells from 51.0% to 15.8%, which is consistent with the immunofluorescence results. Finally, western blot analysis was performed to confirm the results of the other expression assays. As shown in Fig. 4g, P-gp expression dramatically reduced in MDR SCG 7901/VCR cells after incubation with DXS@NPs. These results indicate that the down-regulation of P-gp plays an important part in overcoming cancer MDR and improving the effectiveness of chemotherapy.

3.4. MRI imaging of DXS@NPs in vitro and in vivo

With SPIO loading, the DXS@NPs system becomes a potential candidate for MRI imaging. At first, the T_2 enhancing effect of DXS@NPs on cells was evaluated. After 24 h incubation, the cells were harvested and dispersed in 1% agarose for imaging on a 9.4 T small animal MRI scanner. The results indicate that T_2 signal decreased dramatically with DXS@NPs treatment (Fig. 5a). The visualization of drug delivery in vivo is an important aspect of multifunctional DDSs. Since DXS@NPs was an excellent MRI contrast agent in T_2-weighted MR imaging in vitro, in vivo MR imaging was performed to confirm drug accumulation in the tumor region. In our experiment, MR images of tumor areas were obtained before and after intravenous injection of DXS@NPs (Fig. 5b). The acquired T_2-weighted MR images showed a strong darkening effect in the tumor areas, confirming the successful accumulation of the

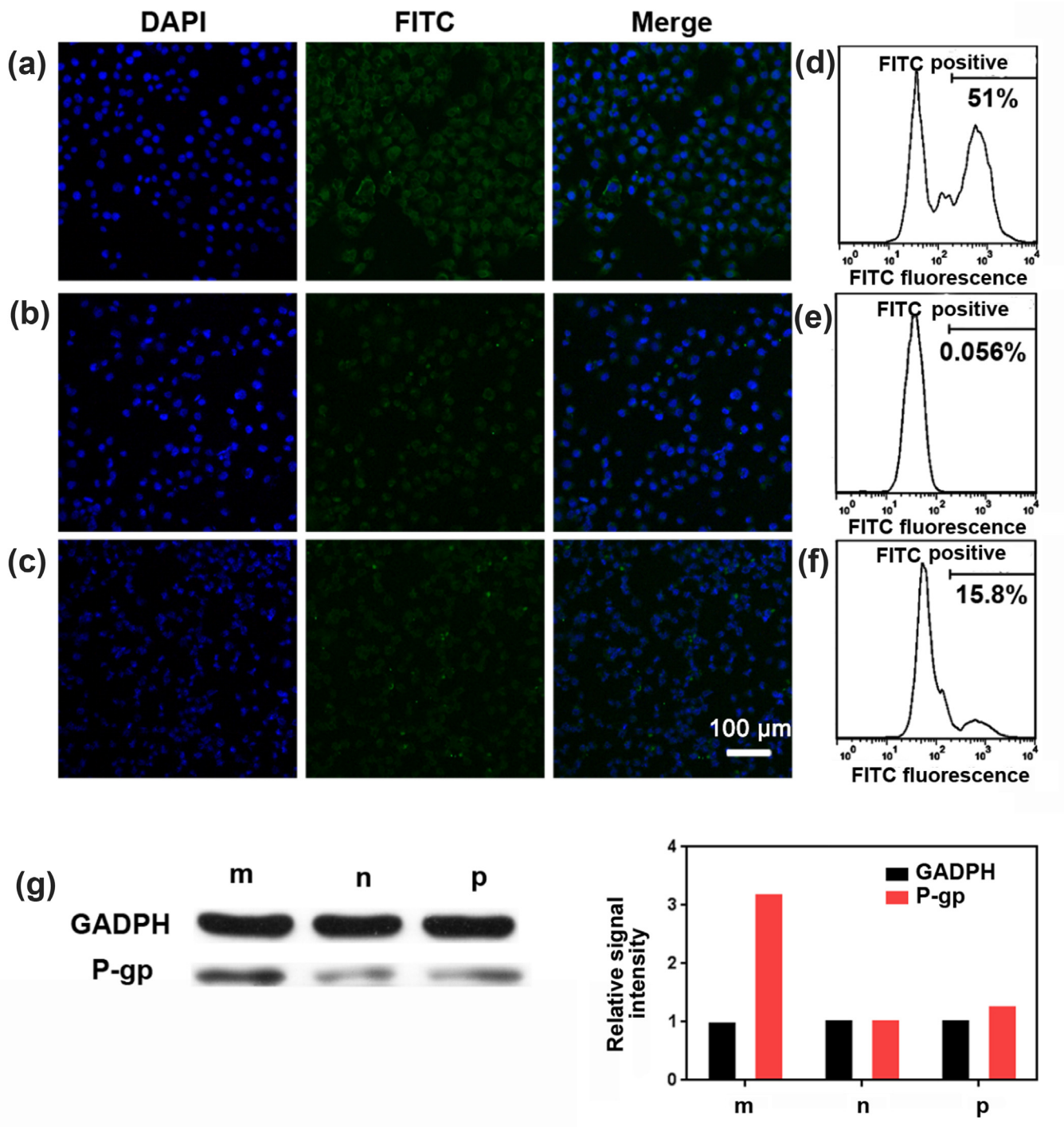

Fig. 4. (Color online) The detection of P-gp in SCG 7901/VCR cells (a,d,**m**), SCG 7901 cells (b,e,**n**) and DXS@NPs-treated SCG 7901/VCR cells (c,f,**p**) by immunofluorescence (a,b, c), flow cytometry (d,e,f) and western blot (g). The optical density (OD) values in each group in western blot were self-normalized for comparison. Scale bar: 100 μm.

nanoparticles. The 36% reduction in signal intensity around the tumor area (Fig. 5c) was also indicative of a high amount of nanoparticle accumulation.

3.5. Anticancer effect in resistant SCG 7901/VCR xenograft

The in vivo therapeutic efficacy of DXS@NPs was investigated by monitoring the tumor growth rates after 15 d of treatment. Four groups ($n = 5$) of nude mice with xenografts of SCG 7901/VCR tumors were used in the following experiments. As shown in Fig. 6a and b, the tumor volumes in the PBS group significantly increased in 15 d. Similar to the control group (PBS), nanoparticles containing only XMD8-92 and SPIOs (XS@NPs) could not delay tumor expansion, while free DOX and DXS@NPs induced a notable inhibition of the tumor growth ($P < 0.01$, one-way ANOVA). Mice treated with DXS@NPs showed a significantly stronger anticancer effect than free DOX group ($P < 0.01$, one-way ANOVA), indicating that DXS@NPs had a necrotic effect on MDR tumors. Histological analysis of the tumors confirmed the tumor necrosis induced by DXS@NPs (Fig. 6c). The antitumor effect of the DXS@NPs described here may be explained by the following reasons. First, XMD8-92 down-regulated P-gp expression, resulting in more DOX being

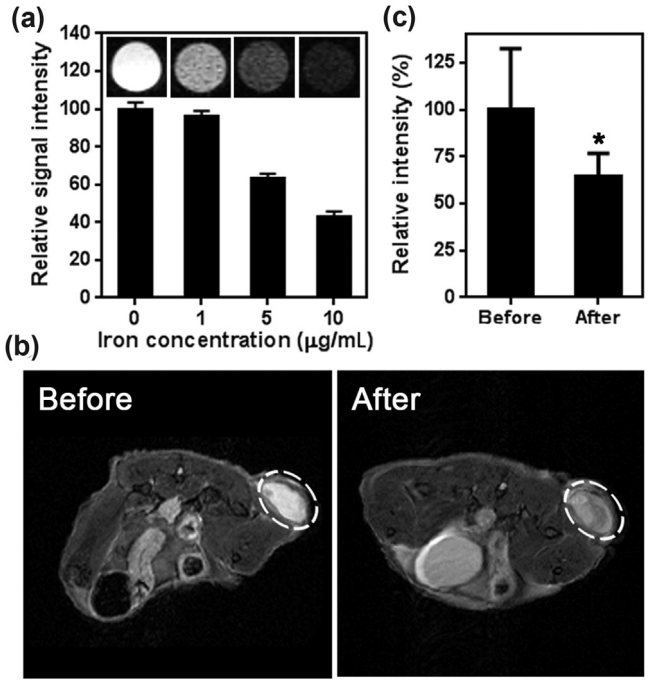

Fig. 5. MRI of DXS@NPs in vitro and in vivo. (a) In vitro T_2 enhancing effect on SCG 7901/VCR cells after DXS@NPs incubation. (b) In vivo MRI before and after DXS@NPs intravenous injection. (c) Histogram of the reduction of relative MRI signals intensity in tumor regions.

trapped within the tumor cells. Second, the biotin modification on the surface of DXS@NPs enhanced the targeted drug delivery into the cancer cells and contributed greatly to the improved chemotherapeutic effect. Third, the proper diameter of DXS@NPs (91 nm) endowed it with a potent EPR effect, which combined with the biotin-mediated active targeting to enhance drug accumulation at the tumor sites. Finally, the DDS decreased the drug concentration in the bloodstream and the pH-dependent drug release was helpful to increase the drug concentration in the tumor area.

The P-gp expression in tumors from mice treated with PBS, free DOX, XS@NPs, and DXS@NPs was assessed by immunohistochemical methods (Fig. 6d, e). In the PBS-treated group, P-gp was highly expressed on the tumor tissues, while the expression was remarkably reduced in the DXS@NPs group ($P < 0.01$, one-way ANOVA). The other two groups (free DOX and XS@NPs) were still positive for P-gp after two weeks of treatment, but the expression levels were notably lower compared to the control PBS-treated group. The XMD8-92 in the XS@NPs group decreased P-gp expression, while mice in the free DOX-treated group showed reduced cancer cells as well as relatively low P-gp expression. These results demonstrated that DXS@NPs can effectively inhibit SCG 7901/VCR tumor growth likely by reducing its P-gp expression and thereby improving the DOX-induced apoptosis on cancer cells.

3.6. Systemic toxicity

Although mice exposed to free DOX alone showed noticeable tumor growth inhibition compared to the control group, it was accompanied by obvious toxic side effects as well. In our

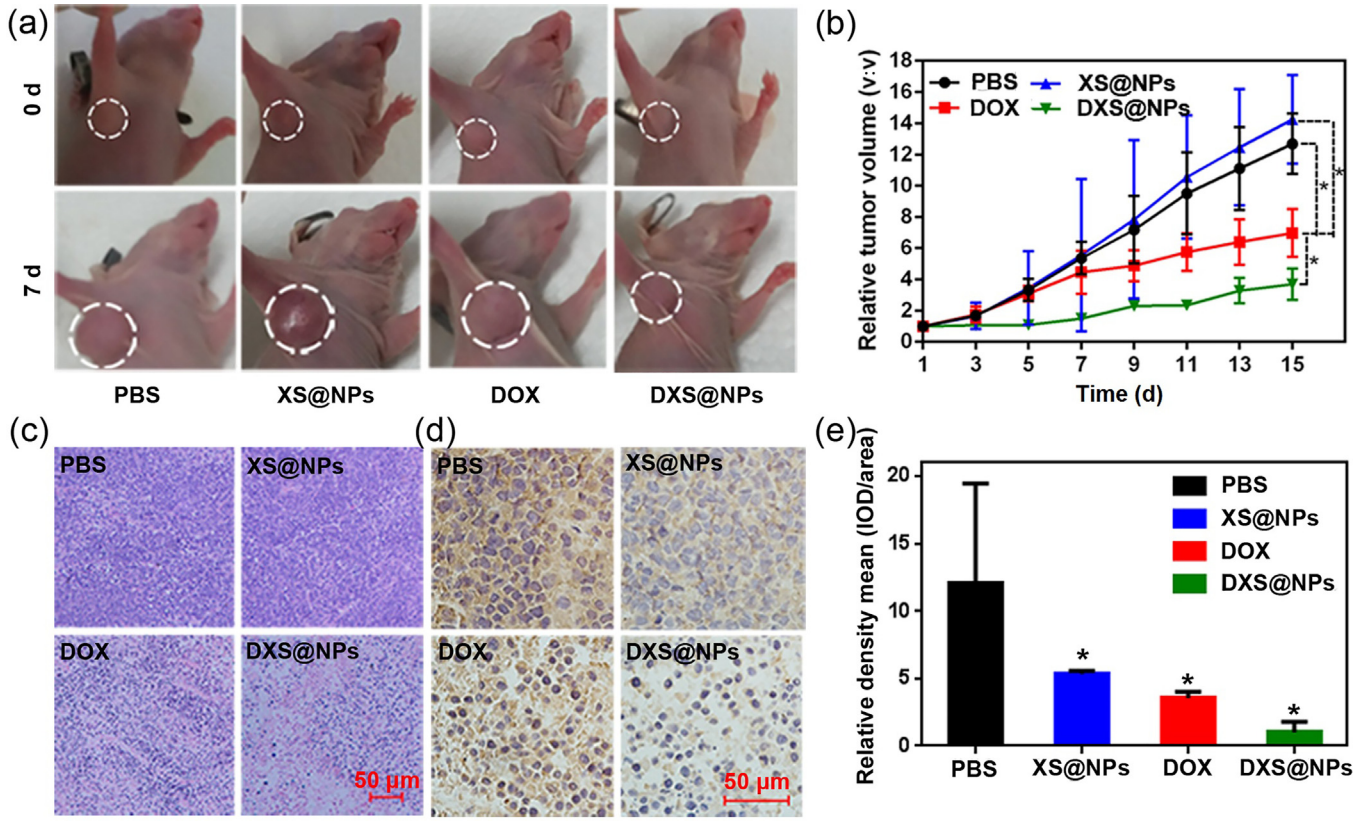

Fig. 6. (Color online) In vivo antitumor efficacy of DXS@NPs in the SCG 7901/VCR tumor-bearing mice. (a) Digital photos, (b) tumor growth profiles and (c) histology analysis of tumors of four groups of mice. Scale bar: 100 μm. (d) Immunohistochemical analysis and (e) relative density mean of P-gp expression in tumors from mice treated with PBS, XS@NPs (XMD8-92 and SPIO were co-encapsulated into Biotin-PEG-b-Leu), free DOX and DXS@NPs (DOX, XMD8-92 and SPIO were co-encapsulated into Biotin-PEG-*b*-Leu). Scale bar: 50 μm.

experiments, this systemic toxicity was investigated by monitoring the body weight of the mice and histological analysis of the main organs after chemotherapy. During the therapy, the body weight of mice reduced significantly (34.5%) after free DOX treatment, while mice in the control group (PBS) and XS@NPs group were barely affected. The body weight of the mice treated with DXS@NPs also decreased slightly in the first 11 d, likely in response to the high dose of DOX, and then remained stable for the duration of the treatment. Compared to the free DOX-treated group, the weight loss in the DXS@NPs group suggests that the DOX-containing DDS developed here could considerably reduce the systemic toxicity of free DOX at the current dose (Fig. S10 online).

Histological analysis of the major organs after 15 d revealed no obvious difference between the four groups (PBS, XS@NPs, free DOX, and DXS@NPs), except for the heart tissue of the free DOX group. As shown in Figs. S11 and S12 (online), heart section from the DOX group exhibited severe congestion in the myocardial blood vessels (Fig. S11 online) associated with edema of myocardial tissue and increased inflammatory cells (Fig. S12 online). In the other three groups, there was no evidence of myocyte damage.

4. Conclusions

In summary, a polypeptide micelles-mediated theranostic nanoplatform was successfully designed to co-deliver the anticancer drug DOX, the MDR reverser XMD8-92, and the MRI agent SPIO. In addition to the EPR effect, the biotin-modified micelles greatly enhanced the in vivo tumor accumulation of DXS@NPs by active targeting, and the improved drug release in the tumor microenvironment (pH 5.5) further increased the intracellular drug concentration. Benefiting from the ability of XMD8-92 to down-regulate P-gp expression, high MDR tumor regression and low systemic toxicity were observed both in vitro and in vivo. Considering these advantages, this theranostic nanosystem represents a promising strategy to overcome MDR cancer and improve the efficacy of chemotherapy.

Conflict of Interest

The authors declare that they have no conflict of interest.

Acknowledgments

This work was supported by the National Basic Research Development Program of China (2017YFA0205201 and 2018YFA0107301), the National Natural Science Foundation of China (81422023, 81871404, 81603015, U1705281, and U1505221), the Fundamental Research Funds for the Central Universities (20720160065, and 20720150141), and the Program for New Century Excellent Talents in University, China (NCET-13-0502).

Author contributions

Gang Liu, Xiaoyuan Chen, Xianming Deng, Xianzheng Zhang and Caixia Yang designed the project. Caixia Yang, Weihai Chen, Xiaoyong Wang and Gang Liu performed the experiments. Caixia Yang, Xin Pang and Chengchao Chu analyzed the data and wrote the manuscript.

Appendix A. Supplementary data

Supplementary data to this article can be found online at https://doi.org/10.1016/j.scib.2019.04.019.

References

[1] Yan Y, Björnmalm M, Caruso F. Particle carriers for combating multidrug-resistant cancer. ACS Nano 2013;7:9512–7.
[2] Wang F, Wang YC, Dou S, et al. Doxorubicin-tethered responsive gold nanoparticles facilitate intracellular drug delivery for overcoming multidrug resistance in cancer cells. ACS Nano 2011;5:3679–92.
[3] Syed SB, Coumar MS. P-glycoprotein mediated multidrug resistance reversal by phytochemicals: a review of sar & future perspective for drug design. Curr Top Med Chem 2016;16:2484–5.
[4] Fletcher JI, Haber M, Henderson MJ, et al. Abc transporters in cancer: more than just drug efflux pumps. Nat Rev Cancer 2010;10:147.
[5] Zahedi P, De SR, Huynh L, et al. Combination drug delivery strategy for the treatment of multidrug resistant ovarian cancer. Mol Pharm 2011;8:260.
[6] Bai F, Wang C, Lu Q, et al. Nanoparticle-mediated drug delivery to tumor neovasculature to combat P-gp expressing multidrug resistant cancer. Biomaterials 2013;34:6163–74.
[7] Shukla S, Wu CP, Ambudkar SV. Development of inhibitors of ATP-binding cassette drug transporters: present status and challenges. Expert Opin Drug Metab Toxicol 2008;4:205–23.
[8] Yang Q, Liao L, Deng X, et al. Bmk1 is involved in the regulation of p53 through disrupting the PML-MDM2 interaction. Oncogene 2013;32:3156–64.
[9] Rovida E, Di Maira G, Tusa I, et al. The mitogen-activated protein kinase Erk5 regulates the development and growth of hepatocellular carcinoma. Gut 2015;64:1454–65.
[10] Yang Q, Deng X, Lu B, et al. Pharmacological inhibition of BMK1 suppresses tumor growth through promyelocytic leukemia protein. Cancer Cell 2010;18:258–67.
[11] Sureban SM, May R, Weygant N, et al. Xmd8-92 inhibits pancreatic tumor xenograft growth via a DCLK1-dependent mechanism. Cancer Lett 2014;351:151–61.
[12] Deng X, Yang Q, Kwiatkowski N, et al. Discovery of a benzo[e]pyrimido-[5,4-b][1,4]diazepin-6(11h)-one as a potent and selective inhibitor of big map kinase 1. ACS Med Chem Lett 2011;2:195–200.
[13] Chen HB, Gu ZJ, An HW, et al. Precise nanomedicine for intelligent therapy of cancer. Sci China Chem 2018;61:1503–52.
[14] Ji C, Gao Q, Dong X, et al. A size-reducible nanodrug with an aggregation-enhanced photodynamic effect for deep chemo-photodynamic therapy. Angew Chem Int Ed 2018;57:11384–8.
[15] Luo HH, Wang QL, Deng YB, et al. Mutually synergistic nanoparticles for effective thermo-molecularly targeted therapy. Adv Funct Mater 2017;27:1702834.
[16] Cai W, Gao H, Chu C, et al. Engineering phototheranostic nanoscale metal-organic frameworks for multimodal imaging-guided cancer therapy. ACS Appl Mater Interfaces 2017;9:2040–51.
[17] Chen WH, Yang CX, Qiu WX, et al. Multifunctional theranostic nanoplatform for cancer combined therapy based on gold nanorods. Adv Healthcare Mater 2015;4:2247–59.
[18] Zhang P, Zhang L, Qin Z, et al. Genetically engineered liposome-like nanovesicles as active targeted transport platform. Adv Mater 2017;30:1705350.
[19] Wang J, Tao W, Chen X, et al. Emerging advances in nanotheranostics with intelligent bioresponsive systems. Theranostics 2017;7:3915–9.
[20] Chu C, Lin H, Liu H, et al. Tumor microenvironment-triggered supramolecular system as an in situ nanotheranostic generator for cancer phototherapy. Adv Mater 2017;29:1605928.
[21] Huang Y, He L, Song Z, et al. Phycocyanin-based nanocarrier as a new nanoplatform for efficient overcoming of cancer drug resistance. J Mater Chem B 2017;5:3300.
[22] Niazi M, Zakeri-Milani P, Najafi HS, et al. Nano-based strategies to overcome p-glycoprotein-mediated drug resistance. Expert Opin Drug Metab Toxicol 2016;12:1021.
[23] Lin G, Mi P, Chu C, et al. Inorganic nanocarriers overcoming multidrug resistance for cancer theranostics. Adv Sci 2016;3:1600134.
[24] Huang C, Chu C, Wang X, et al. Ultra-high loading of sinoporphyrin sodium in ferritin for single-wave motivated photothermal and photodynamic co-therapy. Biomater Sci 2017;5:1512–6.
[25] Zhang J, Zhang J, Li W, et al. Degradable hollow mesoporous silicon/carbon nanoparticles for photoacoustic imaging-guided highly effective chemo-thermal tumor therapy in vitro and in vivo. Theranostics 2017;7:3007–20.
[26] Zhang J, Yang C, Zhang R, et al. Biocompatible D-A semiconducting polymer nanoparticle with light-harvesting unit for highly effective photoacoustic imaging guided photothermal therapy. Adv Funct Mater 2017;27:1605094.
[27] Liu C, Gao H, Lv P, et al. Extracellular vesicles as an efficient nanoplatform for the delivery of therapeutics. Hum Vacc Immunother 2017;13:2678–87.
[28] Yang C, Lin G, Zhu C, et al. Metalla-aromatics loaded magnetic nanoparticles for mri/photoacoustic imaging-guided cancer hototherapy. J Mater Chem B 2018;6:2528–35.
[29] Li L, Yang X, Hu X, et al. Multifunctional $Cu_{39}S_{28}$ hollow nanopeanuts for in vivo targeted photothermal chemotherapy. J Mater Chem B 2017;5:6740–51.
[30] Liu C, Zhang S, Li J, et al. A water-soluble, nir-absorbing quaterrylenediimide chromophore for photoacoustic imaging and efficient photothermal cancer therapy. Angew Chem Int Ed 2019;58:1638–42.

[31] Wang YY, Deng YB, Luo HH, et al. Light-responsive nanoparticles for highly efficient cytoplasmic delivery of anticancer agents. ACS Nano 2017;11:12134–44.
[32] Ye SY, Rao JM, Qiu SH, et al. Rational design of conjugated photosensitizers with controllable photoconversion for dually cooperative phototherapy. Adv Mater 2018;30:1801216.
[33] Zhang SB, Li JH, Wei J, et al. Perylenediimide chromophore as an efficient photothermal agent for cancer therapy. Sci Bull 2018;63:101–7.
[34] Chinen AB, Guan CM, Ferrer JR, et al. Nanoparticle probes for the detection of cancer biomarkers, cells, and tissues by fluorescence. Chem Rev 2015;115:10530–74.
[35] Tian Y, Jiang X, Chen X, et al. Doxorubicin-loaded magnetic silk fibroin nanoparticles for targeted therapy of multidrug-resistant cancer. Adv Mater 2014;26:7393–8.
[36] Vig BS, Huttunen KM, Laine K, et al. Amino acids as promoieties in prodrug design and development. Adv Drug Delivery Rev 2013;65:1370–85.
[37] Scarano W, de Souza P, Stenzel MH. Dual-drug delivery of curcumin and platinum drugs in polymeric micelles enhances the synergistic effects: a double act for the treatment of multidrug-resistant cancer. Biomater Sci 2015;3:163–74.
[38] Xiong XB, Lavasanifar A. Traceable multifunctional micellar nanocarriers for cancer-targeted co-delivery of MDR-1 sirna and doxorubicin. ACS Nano 2011;5:5202–13.
[39] Lee SM, Kim HJ, Kim SY, et al. Drug-loaded gold plasmonic nanoparticles for treatment of multidrug resistance in cancer. Biomaterials 2014;35:2272–82.
[40] Chen WH, Luo GF, Lei Q, et al. Mmp-2 responsive polymeric micelles for cancer-targeted intracellular drug delivery. Chem Commun 2015;51:465–8.
[41] Li Z, Hu Y, Howard KA, et al. Multifunctional bismuth selenide nanocomposites for antitumor thermo-chemotherapy and imaging. ACS Nano 2016;10:984–97.
[42] Xing R, Bhirde AA, Wang S, et al. Hollow iron oxide nanoparticles as multidrug resistant drug delivery and imaging vehicles. Nano Res 2012;6:1–9.

Caixia Yang received her M.S. degree in 2016 from the Center for Molecular Imaging and Translational Medicine (CMITM) at Xiamen University, under the supervision of Prof. Gang Liu. Currently, she is a Ph.D. candidate at the Chinese University of Hong Kong. Her interests focus on developing nanomaterials for drug delivery and molecular imaging.

Gang Liu received his M.D. degree from North Sichuan Medical College (China) in 2002 and Ph.D. degree from Sichuan University (China) in 2009. Subsequently, He focused his training on nanomedicine and molecular imaging at the National Institutes of Biomedical Imaging and Bioengineering, National Institutes of Health. In 2012, he joined the Center for Molecular Imaging and Translational Medicine, Xiamen University. Currently he is a Full Professor of Biomedical and Bioengineering. His research interests include biomaterials, theranostics, and molecular imaging.